



# HDX-MS finds that partial unfolding with sequential domain activation controls condensation of a cellular stress marker

Ruofan Chen<sup>a</sup>, Hendrik Glauninger<sup>b,c</sup> , Darren N. Kahan<sup>b</sup> , Julia Shangguan<sup>b</sup>, Joseph R. Sachleben<sup>d</sup>, Joshua A. Riback<sup>b,c,1</sup>, D. Allan Drummond<sup>b,e</sup> , and Tobin R. Sosnick<sup>a,b,e,2</sup>

Edited by William DeGrado, University of California San Francisco, San Francisco, CA; received December 12, 2023; accepted January 29, 2024

Eukaryotic cells form condensates to sense and adapt to their environment [S. F. Banani, H. O. Lee, A. A. Hyman, M. K. Rosen, *Nat. Rev. Mol. Cell Biol.* **18**, 285–298 (2017), H. Yoo, C. Triandafillou, D. A. Drummond, *J. Biol. Chem.* **294**, 7151–7159 (2019)]. Poly(A)-binding protein (Pab1), a canonical stress granule marker, condenses upon heat shock or starvation, promoting adaptation [J. A. Riback *et al.*, *Cell* **168**, 1028–1040, e19 (2017)]. The molecular basis of condensation has remained elusive due to a dearth of techniques to probe structure directly in condensates. We apply hydrogen–deuterium exchange/mass spectrometry to investigate the mechanism of Pab1’s condensation. Pab1’s four RNA recognition motifs (RRMs) undergo different levels of partial unfolding upon condensation, and the changes are similar for thermal and pH stresses. Although structural heterogeneity is observed, the ability of MS to describe populations allows us to identify which regions contribute to the condensate’s interaction network. Our data yield a picture of Pab1’s stress-triggered condensation, which we term sequential activation (Fig. 1A), wherein each RRM becomes activated at a temperature where it partially unfolds and associates with other likewise activated RRMs to form the condensate. Subsequent association is dictated more by the underlying free energy surface than specific interactions, an effect we refer to as thermodynamic specificity. Our study represents an advance for elucidating the interactions that drive condensation. Furthermore, our findings demonstrate how condensation can use thermodynamic specificity to perform an acute response to multiple stresses, a potentially general mechanism for stress-responsive proteins.

condensate | Pab1 | hydrogen exchange | mass spectrometry | phase separation

Cells form cytosolic clusters of RNA and RNA-binding proteins in response to stress (1–4). These clusters, termed stress granules when microscopically visible, fall into the category of biomolecular condensates. Studies investigating the molecular basis of condensation typically focus on low complexity regions (LCRs) and intrinsically disordered regions (IDRs) that mediate weak multivalent interactions to drive condensation (5–8). Yet in important physiological cases, such as for the core stress granule marker poly(A)-binding protein (Pab1 in yeast), condensation is mediated by its folded domains (Fig. 1) (9).

Pab1 is recruited to stress granules across a range of stresses, including heat shock, starvation, as well as oxidative and osmotic stress (1, 2). In nonthermal stresses, stress-induced intracellular acidification acts as a second messenger to trigger condensation (8–11). Accordingly, upon heat shock or starvation-induced acidification, Pab1 autonomously condenses even before stress granule formation (9). The resulting condensates are irreversible by cooling (*SI Appendix*, Fig. S1A) but can be dispersed by stress-induced molecular chaperones orders of magnitude faster than misfolded proteins (12).

Mimicking its *in vivo* behavior, purified Pab1 condenses *in vitro* above a temperature  $T_{\text{cond}} = 39^\circ\text{C}$  (at pH 6.4) or below pH 5.4 (at 30 °C), both of which overlap with *in vivo* stress conditions. The marker smoothly integrates these two signals into a single-phase boundary (Fig. 2A) (9). Notably, the condensation of Pab1 is adaptive with suppression of its condensation reducing cellular fitness during stress (13, 14). However, crucial questions remain related to the structural basis for condensation and the integration of thermal and pH signals.

A major challenge for structural studies of biomolecular condensates is that the process itself interferes with most solution-based techniques including NMR, which requires rapid molecular tumbling (15). Hydrogen–deuterium exchange/mass spectrometry (HDX–MS), however, can probe the H-bond network in insoluble milieus (16). HDX occurs when an H-bond is transiently broken, and the backbone amide proton becomes exposed and exchanges with solvent deuterons. Typically, the ratio of the rate of exchange for an exposed

## Significance

Bimolecular condensation plays a role in many cellular processes. Despite considerable progress, a residue-level description of condensates has been lacking as obtaining high-resolution structural information is impeded by the condensation process itself. We overcame this issue by applying hydrogen–deuterium exchange/mass spectrometry (HDX–MS) to a canonical stress granule marker protein. We propose a sequential activation model where each domain is activated at different temperatures, executes partial unfolding, and associates only with other similarly activated domains to form the condensate, a mechanism we term thermodynamic specificity. The stress marker undergoes the same structural events upon pH- or heat-induced condensation, providing a unifying molecular portrait of stress response with the marker as a central sensor across different stresses.

Preprint servers: Manuscript was deposited to biorxiv.org (<https://doi.org/10.1101/2022.9.21.508844>).

The authors declare no competing interest.

This article is a PNAS Direct Submission.

Copyright © 2024 the Author(s). Published by PNAS. This article is distributed under Creative Commons Attribution-NonCommercial-NoDerivatives License 4.0 (CC BY-NC-ND).

<sup>1</sup>Present address: Department of Molecular and Cellular Biology, Baylor College of Medicine, Houston, TX 77030.

<sup>2</sup>To whom correspondence may be addressed. Email: trsosnick@uchicago.edu.

This article contains supporting information online at <https://www.pnas.org/lookup/suppl/doi:10.1073/pnas.2321606121/-DCSupplemental>.

Published March 21, 2024.

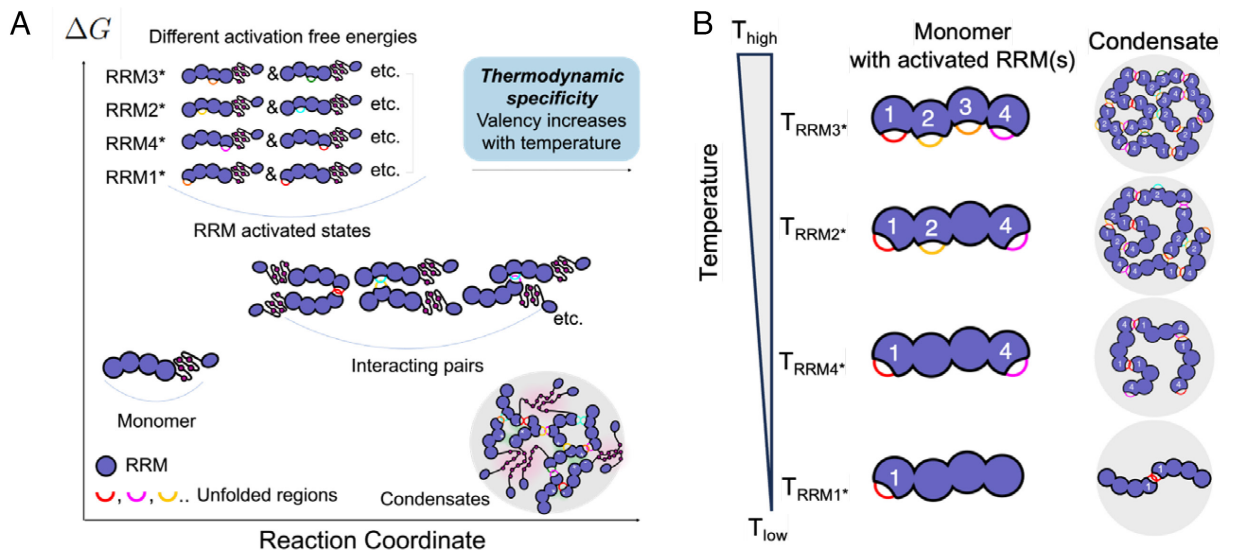


**Fig. 1.** Pab1 condensation, sequential activation, and thermodynamic specificity. (A) When the temperature is increased, the four RRMs become sequentially activated, reflecting each one's proclivity to partially unfold and interact. The activated RRMs are less populated and hence have higher free energies than the nonactivated monomers. Typically, RRM1 is activated first while RRM3 is last. Different colors of unfolded regions illustrate the structural heterogeneity. (B) With thermodynamic specificity, activated RRMs interact with other similarly activated RRMs to create a stable network. Upon activation of additional RRMs, the valency increases, and the condensate morphology can change. Each domain may have multiple activated regions capable of forming interdomain reactions, but only one is shown for simplicity.

amide proton (termed the intrinsic or chemical rate  $k_{\text{chem}}$ ) relative to the observed rate provides information on the “open-to-close” equilibrium according to  $K_{\text{eq}} + 1 = k_{\text{chem}}/k_{\text{obs}} = PF$ , the protection factor (17, 18). When coupled to mass spectrometry, HDX is a powerful method to study the stability and structure of condensates with near-residue level resolution (17). A previous study measured the HDX of monomeric  $\alpha$ -synuclein and probed the correlation between monomeric structural dynamics and the corresponding aggregation kinetics under various conditions (19). Nevertheless, the structure of the condensate itself remained unassessed.

Recent progress in employing cross-linking-MS (XL-MS) to map interactions in the condensates revealed that chaperone HspB8 protects FUS condensates by binding to its RRM domain (20). Another XL-MS study was able to distinguish and quantify intra- and inter-protein interactions in  $\alpha$ -synuclein condensates by equimolar mixing of  $^{14}\text{N}$ - and  $^{15}\text{N}$ -labeled proteins and revealed a shift from a hairpin structure to an elongated conformation upon condensation (21). In a study of the LCR domain of TDP-43, hydroxyl radical protein footprinting (HRPF) identified methionines involved in forming cross- $\beta$  structures in droplets (22). A more recent study utilizing native ion mobility MS of hnRNP condensates formed by different proteins reveals divergent conformational changes upon condensation. Specifically, FUS undergoes a disordered-to-compact transition, whereas TDP-43 remains partially disordered and oligomerizes (23). While powerful, these MS-based strategies provide limited structural and thermodynamic information, and some require covalent modification of the protein. In contrast, HDX-MS obtains this information for nearly every residue in a more uniform manner with minimal perturbation (24).

Here, we apply HDX-MS to identify the factors that enable Pab1 to transduce physiological cellular stress signals into condensation. We find that with temperature or acidification, specific regions of the four RRMs transiently unfold and associate with other similarly activated RRMs. With a further increase in temperature, additional regions of the RRMs become activated one after the other, which promotes further condensation in a process we term sequential activation (Fig. 1).

## Results

In this section, we describe the primary evidence for sequential activation: i) HDX-MS data that identify which regions in the four RRMs undergo partial unfolding in the condensate; ii) NMR data, which demonstrate that the individual RRM constructs remain folded under condensation conditions, implying that transient (high energy) unfolding events initiate the condensation process; and iii) protein engineering studies that identify which RRMs have the biggest influence on condensation.

**HDX-MS Measurements.** We applied HDX-MS to monomeric Pab1 and to condensates generated by heating (39 to 46 °C) or acidification (pH 4.5) (Fig. 2A). Samples were diluted 29-fold into D<sub>2</sub>O buffer (pD<sub>corrected</sub> 6.0, on ice, where pD<sub>corrected</sub> = pD<sub>read</sub> + 0.4) to initiate deuterium labeling. After 30 to 24,000 s of labeling, HDX was quenched, and the condensates were solubilized with 8 M urea (*SI Appendix*, Fig. S2A) and injected into an LC-MS with an in-line protease column (25, 26). Our peptide map had 99% sequence coverage with an average of seven peptides covering each residue, indicating that Pab1 is well suited for HDX-MS studies (*SI Appendix*, Fig. S2B and Table S1).

For monomeric Pab1, the HDX pattern matched the structural boundaries of Pab1's six domains (Fig. 2B). Peptides from the five structured domains exchanged with  $k_{\text{obs}}$  considerably slower than peptides from the disordered regions, which included the N and C termini, interdomain linkers, and the P domain, which is a proline-rich IDR next to RRM4. These disordered regions generally exchanged with an observed rate matching that of an unstructured protein,  $k_{\text{obs}} \sim k_{\text{chem}}$ , implying that these regions lack stable H-bonds.

However, the four RRMs had different exchange rates, indicating that they have different stabilities. For RRM1, 2, and 4, the slowest peptides exchanged with a  $PF \sim 10^3$  to  $10^5$  (Figs. 2B and 3 and *SI Appendix*, Fig. S3). This high degree of protection is consistent with a stability  $\Delta G_{\text{HX}} = RT \ln PF \sim 4$  to 7 kcal mol<sup>-1</sup>. Many of the peptides from RRM3 exchanged even slower and had less than 50% deuteration level even after 24,000 s (Figs. 2B and 3 and *SI Appendix*, Fig. S3). Accordingly, we estimate the

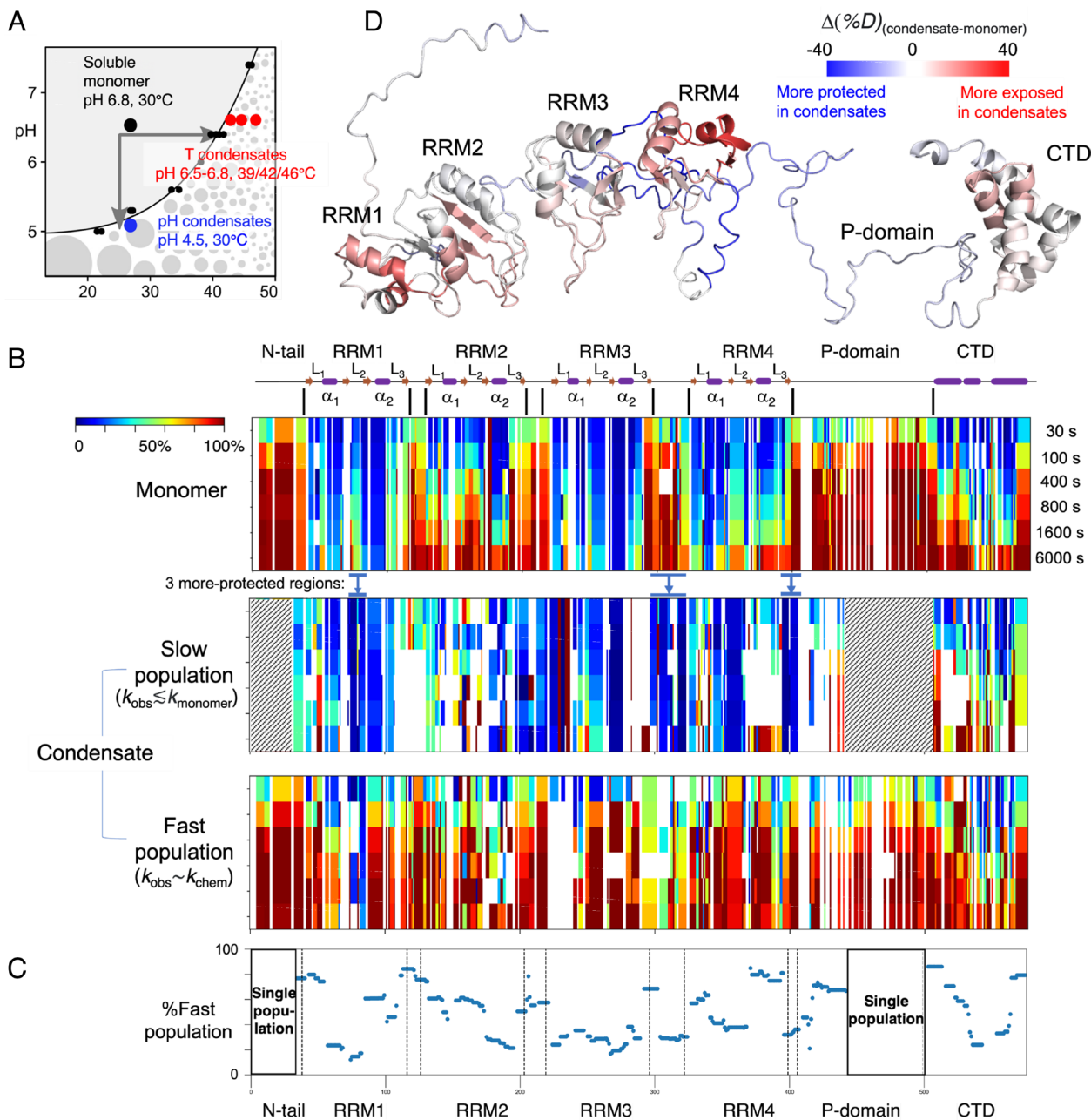


**Fig. 2.** HDX of the monomer and condensate. (A) Conditions for obtaining temperature- and pH-induced condensates are based on Pab1's phase diagram (adapted from ref. 9). (B) HDX heat map for monomeric (Top) and 46 °C-condensed Pab1 decomposed into the map for the slow (Middle) and the fast populations (Lower) using HDExaminer's bimodal fitting routine. The horizontal axis represents Pab1 sequence, and the vertical axis is increasing exchange time. Color represents the level of deuterium uptake. The white spaces in the Middle panel represent regions where the bimodal analysis could not confidently separate the two subpopulations with reasonable uptake profiles for both. The N-terminal tail and part of the P domain remain unimodal in the condensates (spaces with diagonal lines). Domain boundaries and secondary structures are depicted in the plot (rectangles for helices, arrows for strands). (C) The percentage of the fast population for each residue calculated as the average of %Fast for the three shortest peptides covering each residue. The map of %Fast analyzed on a peptide level for the RRMs is in *SI Appendix*, Fig. S6. (D) %D difference between 46 °C condensates and monomer at  $t_{\text{HDX}} = 100$  s mapped onto the Pab1 structure. Structure generated with Raptor-X (27). HDX data were reproducible across 2 bioreplicates (*SI Appendix*, Fig. S2C).

stability of RRM3 to be greater than 7 kcal mol<sup>-1</sup>, making it the most-stable RRM, a property that was later found to reduce its relative involvement in the condensation process compared to the other RRMs.

**Partial Unfolding in Condensates.** Having established the baseline behavior, we probed the effects of condensation on Pab1's HDX pattern. We observed an extensive change with regions exchanging both faster or slower than in the monomer, reflecting both destabilization and stabilization, respectively (Fig. 2 B–D and *SI Appendix*, Figs. S3 and S4). Less change in HDX was observed

for the P domain and C-terminal domain (Fig. 2D and *SI Appendix*, Fig. S3), consistent with Pab1 condensation being mostly mediated by the RRMs and the contributions of the P-domain involving hydrophobic side-chains (9).

Depending on the RRM, destabilized regions contained helices, hairpins, and β-strands (Figs. 2D and 3 and *SI Appendix*, Figs. S3 and S4). Most of the destabilization observed in RRM1 and RRM4 occurred in the α2 helical region and L1 hairpin, whereas most of the destabilization observed in RRM2 occurred at the L1 and L2 hairpins (Fig. 2D and *SI Appendix*, Figs. S3 and S4). Some β-strands also were destabilized (Fig. 2D and *SI Appendix*, Fig. S3),

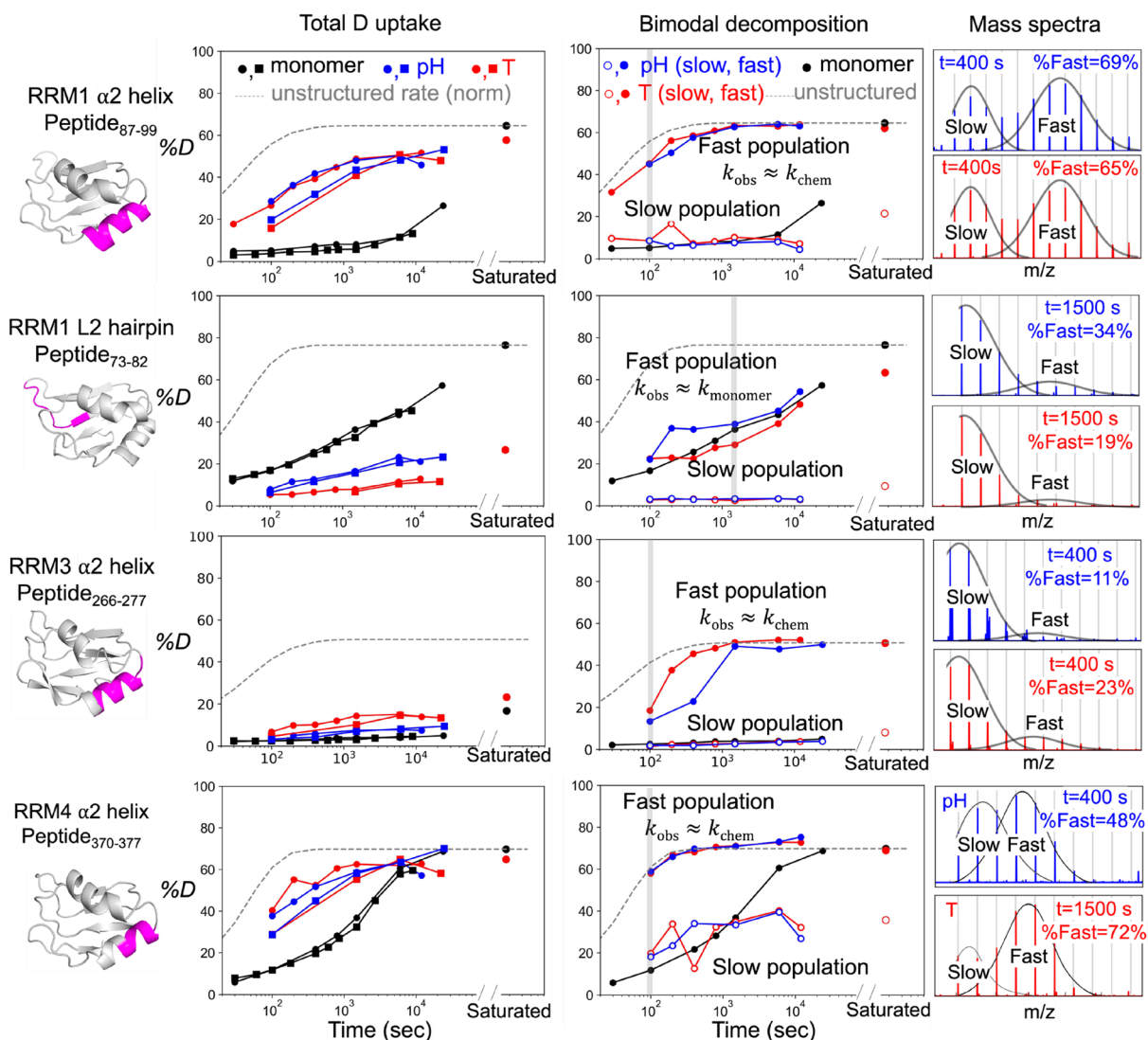


**Fig. 3.** Heterogeneity and D uptake curves of RRM1  $\alpha$ 2-helix, L2 hairpin and RRM3, RRM4  $\alpha$ 2-helices. The total uptake curve combines the fast and slow populations with data from two replicates shown. The bimodal fitting procedure extracts individual D uptake curves for the fast and the slow populations. The unstructured rate ( $k_{\text{chem}}$ ) is normalized to the back exchange level. For the regions shown, the mass spectrum envelopes indicating two (or more) different populations are obtained at 400, 1,500, 400, and 400 s, respectively, where the two populations are well separated. Data from one of the two replicates are shown for simplicity in the bimodal decomposition panel. Corresponding plots for RRM2  $\alpha$ 2-helix and other discussed regions are presented in *SI Appendix*, Fig. S5.

which may explain the previous finding that RNA is ejected from Pab1 upon condensation (9), as the  $\beta$  strands are directly involved in RNA binding (28). Compared to the other RRMs, the deuterium uptake of RRM3 was closer to that of the monomeric state (*SI Appendix*, Figs. S3 and S4), implying condensation had less of an effect on this RRM.

Regions that had increased stability upon condensation included the linkers, P domain, and L2 hairpin region of RRM1 (Figs. 2 B and D and 3 and *SI Appendix*, Figs. S3–S5). The linker between RRM3–RRM4 (Res<sub>303–315</sub>), and that between RRM4 and P domain (Res<sub>392–407</sub>), which were unstructured in monomers, became over 100-fold more protected (*SI Appendix*, Figs. S3 and S5), suggesting that they fold and form stable H-bonds in the condensates. Notably, the L2 hairpin in RRM1 (Peptide<sub>73–82</sub>) also became more protected, which could be due to the hairpin remaining native-like but with additional interactions, or it could adopt a new structure in the condensate. HDX also was slowed for a region of the P domain containing eight contiguous alanine residues, potentially due to them having adopted a helical structure (Peptide<sub>418–442</sub>, *SI Appendix*, Fig. S5).

#### Considerations in the Interpretation of the Multiple Peaks in the HDX Data.

Whereas all peptides in the monomer had a single mass envelope, indicative of a single population, numerous peptides from the condensate had multiple peaks (Fig. 3, mass spectra). We first considered whether the multiple peaks could be due to incomplete removal of monomers from the condensate sample, which was obtained by centrifugation and the removal of the supernatant by pipetting. This potential contamination was ruled out by the existence of numerous peptides that lacked a mass envelope that corresponds to the monomer which would be expected if there were residual monomer in the supernatant.

We next considered whether the multiple peaks could be due to exchange occurring in the EX1 limit, as is frequently assumed when multiple peaks are observed. EX1 behavior occurs when  $k_{\text{chem}} \gg k_{\text{close}}$  so that concerted D uptake occurs across multiple sites when a region unfolds for the first time (*SI Appendix*) (24). This concerted uptake would produce a second peak at a mass value higher by the number of exchanging sites. Critically, when exchange is in the EX1 limit, the envelope at lower mass should decrease in amplitude while the envelope at the higher mass should

increase by the same amount as the population shifts from the initial (protonated) to the final (deuterated) state. However, the condensate data did not display this population shift. Instead, the peak heights remained relatively constant over the labeling period. Accordingly, we conclude that the presence of multiple peaks in the condensate data is not due to HDX occurring in the EX1 limit or residual monomer levels. Rather, the multiple peaks are attributable to the presence of structurally distinct, noninterconverting populations with HDX occurring in the EX2 limit.

To explore this heterogeneity, a bimodal analysis was conducted specifically to estimate the population fractions and obtain the HDX build-up curves for the faster and slower populations (Fig. 2*B*). The faster population has much less protection while the exchange of the slower population generally is very similar to that of the monomer (Fig. 2*B*). For the RRM1 L2 hairpin region (Peptide<sub>73-82</sub>) with heightened protection likely from newly formed interactions, exchange for both its faster and slower populations were slower than  $k_{\text{chem}}$  being close to, or even slower than the rate in the monomer (Figs. 2*B* and 3).

The percentage of the population that exchanged at essentially the unfolded rate ( $k_{\text{chem}}$ ) varied throughout the 4 RRM domains (Fig. 2*C* and *SI Appendix*, Fig. S6). Regions that possessed the largest fast-exchanging population were the  $\alpha$ 2-helices of RRM1 and 4, where the fast fraction was ~65% and 80% of the population, respectively (Figs. 2*C* and 3 and *SI Appendix*, Fig. S6). For the most-stable RRM3, the fast-exchanging fraction was under 30% for all peptides (Fig. 2*C* and *SI Appendix*, Fig. S6), indicating that this RRM experienced the least destabilization upon condensation. In sum, the HDX data indicate that Pab1 molecules are structurally heterogeneous in the condensate, and they can adopt alternative, sometimes partially unfolded conformations and/or form a variety of new interchain interactions.

**Testing Sequential Activation.** A major element of our model is that at lower temperatures, the least-stable RRM domains should preferentially be involved in condensation as they are most activatable, but at higher temperatures, the more-stable RRM domains should become activated and play a heightened role in the condensation process. We tested this prediction by conducting HDX measurements on condensates formed at three temperatures, 39, 42, and 46 °C (Fig. 2*A* and *SI Appendix*, Fig. S7). To visualize the temperature dependence, we plotted the difference between D uptake for condensates formed at 39 versus at 42 °C and between those formed at 42 versus at 46 °C. Indeed, we find that the condensate created at 42 °C has higher D uptake than the condensates formed at 39 °C, with RRM3 having the least increase in uptake (*SI Appendix*, Fig. S7A). In addition, the behavior of RRM3 diverged from other RRM domains with only RRM3 exhibiting an increase in D uptake in the condensates formed at 46 °C as compared to condensates formed at 42 °C (*SI Appendix*, Fig. S7*A* and *B*). Furthermore, the fast-exchanging subpopulation for RRM3 also increased at higher temperatures for RRM3 (*SI Appendix*, Fig. S7*C*), providing additional support for sequential activation.

**Acid-Induced Condensates.** The pH-triggered condensation is promoted by acidification of the 49 glutamates, 29 aspartates, and 9 histidines (15% charged of total residues) (*SI Appendix*, Fig. S8). To investigate how Pab1 integrates thermal and acidification stress signals into one phase boundary, we compared Pab1's HDX behavior when exposed to these conditions. In terms of both total D uptake and heterogeneity, pH and temperature had very similar effects (Fig. 4*A* and *SI Appendix*, Fig. S9). For regions with heterogeneity, the averaged %D differences between the pH and

T condensates were  $0.3 \pm 10\%$  and  $-0.4 \pm 8.3\%$  for the slow- and fast-exchanging subpopulation, respectively (averaged across all peptides and time points, *SI Appendix*, Fig. S9). However, the D uptake is higher in pH-induced condensates for residues 392 to 407 (Fig. 4*A*), comprising the linker between RRM4 and the P domain, one of the regions that experienced the most substantial increase in D uptake upon condensation (Fig. 2 *B* and *D* and *SI Appendix*, Fig. S3). This RRM4-P linker contains 4 positively charged residues but no histidines and also is an unalignable region in the Pab1-orthologs' multiple sequence alignment (9). Nevertheless, the overall similarity in the HDX indicates that the condensation of Pab1 results from similar structural changes in response to temperature and acidification allowing for a unified response with Pab1 being a central sensor (29).

**RRMs Are Individually Stable at Elevated Temperatures.** To investigate whether the disorder observed in the condensates reflects the intrinsic stability of each domain, we collected individual <sup>1</sup>H-<sup>15</sup>N HSQC spectra for RRM1, 2, and 3 at 35 and 45 °C, which are below and above Pab1's T<sub>cond</sub> of 39 °C, respectively (at pH 6.8). At both temperatures, the NMR spectra for the three individual RRM domains remained well dispersed, the hallmark of a folded protein, and were nearly unchanged with no evidence of any conformation change upon heating (Fig. 4*B* and *SI Appendix*, Fig. S10*A*). Furthermore, the peak volumes did not measurably decrease, implying all the protein molecules stayed in solution, as determined by a comparison between the area of the methyl and reference compound (trimethylsilylpropanoic acid) peaks (*SI Appendix*, Fig. S10*B*). For RRM1, the most dynamic RRM by HDX, the NMR T<sub>1</sub>/T<sub>2</sub> relaxation measurements, which are sensitive to tumbling rates (15), were similar at the two temperatures (*SI Appendix*, Fig. S10*C*). Further, the relaxation measurements yielded an estimated molecular weight of  $9.35 \pm 0.42$  kDa at 35 °C and  $8.54 \pm 0.97$  kDa at 45 °C, close to RRM1's molecular weight of 9.6 kDa, implying that it remains monomeric. Also, in the NMR water saturation transfer HDX measurements [CLEANEX (30)] at 45 °C, no new peaks appeared that could be associated with rapid HDX and disorder (Fig. 4*B* and *SI Appendix*, Fig. S10*A*). Finally, at pH 5.2 (0.2 units below pH<sub>cond</sub> at 30 °C), RRM1's spectrum likewise remained similar to its pH 6.8 spectrum (*SI Appendix*, Fig. S10*D*). In summary, the three individual RRM domains remained folded under conditions where Pab1 condenses.

This finding implies that the structural changes observed in the condensates were conditional on the formation of new inter-RRM contacts stabilizing otherwise transient and unstable (higher energy) partially unfolded conformations (Fig. 1*A*). In other words, the condensate formed from rare, partially unfolded states populated enough by stress that they can form a critical nucleus and grow via a (diffusion-limited) addition of other rare conformations (31, 32). Evidence of the presence of such partially unfolded states that escape detection by NMR measurements comes from numerous HDX studies where exchange occurs much faster than expected if exchange requires global unfolding (33, 34). Rather, HDX occurs from partially unfolded states that have lower free energy than the globally unfolded state. Overall, our findings point to a condensation mechanism that involves the presence of otherwise unstable, partially unfolded states forming a network of H-bonds stabilized by inter-RRM interactions within the condensate.

**RRMs Have Different Activation Temperatures.** The different patterns of HDX suggested that RRM domains participated differently in the condensation process. Specifically, RRM3 remained largely folded with a native-like HDX pattern, whereas RRM1, 2, and 4

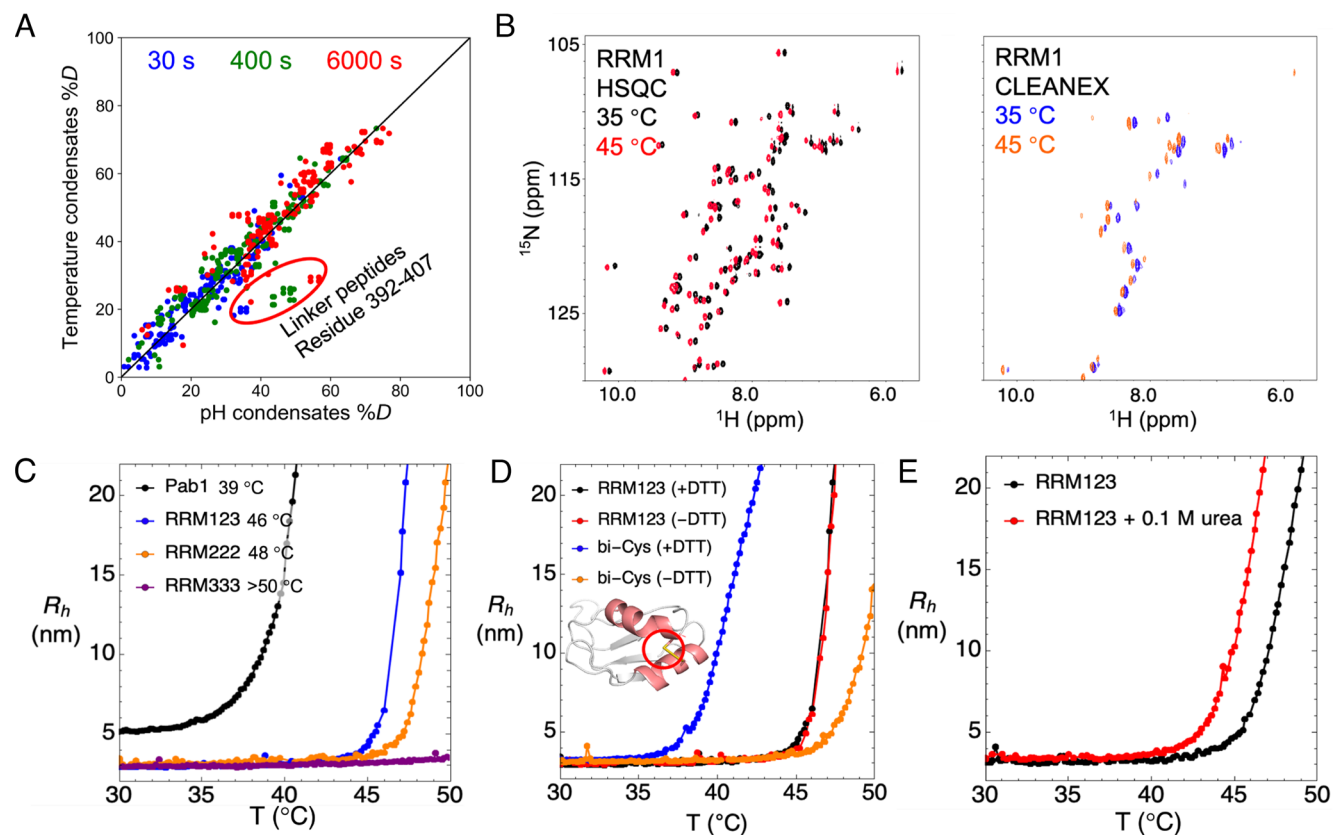


**Fig. 4.** NMR and protein engineering studies support a sequential activation model for Pab1 condensation. (A) Scatter plot comparing the deuterium uptake of pH and temperature condensates at  $t_{\text{HDX}} = 30, 400$ , and  $6,000$  s. (B) NMR of the individual RRM1 domain taken at  $35$  and  $45^\circ\text{C}$ , pH  $6.8$ . Left is the  $^1\text{H}$ - $^{15}\text{N}$  NMR HSQC spectrum, and Right is the corresponding water saturation transfer spectrum that visualizes fast-exchanging sites [CLEANEX (30)]. (C) Condensation temperature measured by DLS. (D) Condensation of the bi-Cys mutant having a disulfide bond between I61C and K94C on RRM1. (E) Condensation of RRM123 in the absence and presence of  $0.1\text{ M}$  urea.

exhibited significant partial unfolding in the condensate formed at  $46^\circ\text{C}$ .

We investigated the extent to which each RRM promoted condensation by comparing the  $T_{\text{cond}}$  measured using dynamic light scattering (DLS) of the WT triplet RRM1–RRM2–RRM3 (RRM123) to engineered triplet RRM constructs, termed RRM111, RRM222, and RRM333, that retained the native linkers. Notably, RRM111 precipitated at room temperature, whereas RRM123 and RRM222 condensed at  $46$  and  $48^\circ\text{C}$ , respectively. RRM333 remained monomeric with an unchanging  $R_h$  out to the highest measured temperature,  $50^\circ\text{C}$  (Fig. 4C). The relative order of  $T_{\text{cond}}$ , RRM111  $\ll$  RRM123  $<$  RRM222  $\ll$  RRM333, largely tracked with the extent of HDX seen in each RMs. These results suggest that each RRM becomes partially unfolded and capable of participating in condensation at a different temperature, typically starting with RRM1. A previous study found Pab1 multimerization to be dependent on RRM1 (35), potentially related to RRM1's role in initiating condensation that we identified here.

**Pab1 Condenses through Interactions between Activated RMs.** Inspired by the proposed role of the nonspecific weak interactions in biomolecular condensation (5–8), we evaluated whether each molecule must contain at least one activated (i.e., partially unfolded) RRM to participate or whether weak interactions are sufficient for an unactivated RRM to participate in condensation. Accordingly, we examined whether triplet RRM constructs (RRM123, RRM222, and RRM333, with  $T_{\text{cond}} = 46, 48$ , and  $>50^\circ\text{C}$ , respectively) would cocondense with Pab1 at  $42$  or  $46^\circ\text{C}$ , temperatures above Pab1's normal  $39^\circ\text{C}$   $T_{\text{cond}}$  but below the  $T_{\text{cond}}$  of all of the triplets. The amount of material that cocondensed

was identified using sodium dodecyl sulfate–polyacrylamide gel electrophoresis (SDS-PAGE) from the fraction in the pellet after centrifugation at  $15,800\text{ g}$  for  $10\text{ min}$ .

When the triplets were mixed with Pab1 at  $42^\circ\text{C}$ , there was little (RRM123, 222) to no (RRM333) measurable amount of triplet in the condensate (*SI Appendix*, Fig. S11). At  $46^\circ\text{C}$  (at or below  $T_{\text{cond}}$  of the triplets), the majority of RRM123 (>50%) and almost all the RRM333 molecules (>90%) remained in the supernatant (*SI Appendix*, Fig. S11). The majority (>50%) of the RRM222 molecules, however, cocondensed with Pab1 (*SI Appendix*, Fig. S11). Here, the increase in cocondensation of RRM222 with temperature points to cocondensation arising from the temperature-dependent domain activation. Moreover, at  $46^\circ\text{C}$ , RRM222 cocondensed to a greater extent compared to RRM123, regardless of its higher  $T_{\text{cond}}$  and less cocondensation at  $42^\circ\text{C}$ . This observation also pointed to cocondensation being influenced by the RRM composition of the construct rather than the effect simply being a concentration effect. We attribute the enhancement of RRM222's cocondensation at  $46^\circ\text{C}$  to it having all three domains on the verge of activation, which helped increase the number of interactions (i.e., valency) that can promote its participation in the condensate. In summary, the cocondensing experiments point to activation being required for an RRM to participate in condensation and that weak interactions are insufficient to recruit an unactivated RRM.

**Unfolding Is a Critical Early Step for Condensation.** A key test of the role of partial unfolding in mediating condensation is that suppressing unfolding should suppress condensation. We targeted RRM1's helices, one of the most labile structures according to HDX–MS. We made a “bi-Cys” variant of RRM123 with a

stabilizing disulfide bond inserted between the two helices (I61C, K94C) but lacking the two endogenous cysteines (Fig. 4D), permitting oxidation-dependent stabilization of these two helices. Under reducing conditions where the disulfide bond was absent (1 mM dithiothreitol, DTT),  $T_{\text{cond}}$  was considerably lower, 39 versus 48 °C. As a control, the  $T_{\text{cond}}$  of WT RRM123 was found to have no dependence on DTT. The WT RRM123's  $T_{\text{cond}}$  was noticeably higher (46 °C) than the reduced bi-Cys version, presumably because the cysteine substitutions themselves were destabilizing (although the variant retained the same  $R_h$  value as its parent, suggesting that it remained folded). Regardless, the large increase in  $T_{\text{cond}}$  upon formation of the disulfide bond indicated that the unfolding of one or both of RRM1's helices helped trigger condensation in RRM123. In addition, the bi-Cys mutant with the disulfide bond had nearly the same  $T_{\text{cond}}$  as RRM222 (SI Appendix, Fig. S1B). This suggests that once RRM1's partial unfolding was inhibited, the onset of condensation is now determined by RRM2, the next domain likely to exhibit partial unfolding.

Further supporting our conclusion that partial unfolding is a necessary step, we found that condensation was promoted by low concentrations of denaturant. The addition of 0.1 M urea reduced  $T_{\text{cond}}$  by 2 °C (Fig. 4E), whereas 1 M urea abolished condensation even though circular dichroism spectroscopy indicates no loss of secondary structure (SI Appendix, Fig. S12). The contrasting effects of denaturant support a model where Pab1's condensation involves an initial partial unfolding step followed by the formation of a network of interchain interactions. The unfolding step is promoted by denaturant, but the subsequent condensate-promoting interactions are also hindered to an increasing degree, with the net effect favoring condensation only at low concentrations of denaturant.

**Inter-RRM Linkers Are Flexible but Inhibitory to Condensation.** Small-angle X-ray scattering (SAXS) measurements found that monomers can be modeled as an ensemble of folded but noninteracting domains connected by flexible linkers (SI Appendix, Fig. S13). The experimental pair-distance distribution function,  $P(r)$ , was similar to that of a simulated noninteracting ensemble, especially as compared to an extended or compact conformation. In addition, the  $P(r)$  was largely unchanged when the interdomain interactions were weakened by adding either 50 to 350 mM NaCl or 0.5 M urea (SI Appendix, Fig. S13 C and D). These results support our modeling of the monomer's ensemble as noninteracting domains and argue against an autoinhibition model where folded RRM domains within the same molecule interact to generate a compact state that inhibits the intermolecular interactions necessary for condensation.

Nevertheless, the replacement of linkers between RRM1–RRM2 and RRM2–RRM3 with glycine-serine or scrambled sequences reduced the  $T_{\text{cond}}$  by ~3 °C (SI Appendix, Fig. S13E). We interpret this result to mean that the native linkers form stabilizing interactions in the native monomer.

## Discussion

Our study creates a unifying molecular portrait of Pab1 condensation. The process is triggered by stress-induced partial unfolding resulting in interaction-prone regions and domain activation. Although mediated by the folded RRM domains rather than the IDR P domain (9), Pab1 condensation conforms to the standard view that disorder and multivalent interactions (usually mediated by LCR/IDR for other condensing proteins) underlie biocondensation.

Our condensate data support the sequential activation of Pab1 wherein each of the RRM domains becomes activated and partially unfolded at a temperature reflecting its own energy surface (Fig. 1A). Generally, RRM1 is the first to activate, while RRM3 is the last. Our NMR studies further indicate that isolated RRM domains remain folded at temperatures above Pab1's  $T_{\text{cond}}$ . Therefore, individually activated RRM domains require additional interactions to remain partially unfolded and form a stable condensate. Such additional interactions can be facilitated by an increase in local concentration occurring as the chain forms more interactions in a maturation or hardening process. This process stabilizes the condensate (6, 36) to the point where it cannot be reversed by cooling (SI Appendix, Fig. S1A).

Because the RRM domains have different activation temperatures and the ability to form stable contacts requires domain activation, the RRM domains will preferentially form contacts with other RRM domains having similar activation temperatures. We term this partner selection thermodynamic specificity. That is, condensation does not depend upon the presence of a highly complementary binding interface that one expects for biomolecular association. Rather, less specific but multivalent interactions between activated RRM domains determine the contact network at any given temperature. With the activation of additional domains at higher temperatures, the interaction valency increases. This increase lowers the percolation threshold and increases the likelihood of forming a system-spanning network (37, 38). In principle, the increase in valency with temperature should lead to an increase in condensate stability and change in morphology, successively changing the ensemble from dimers to 1D chains and then to 2D and 3D networks (Fig. 1B), which may have implications for condensate dispersal by molecular chaperones (12).

Our findings also reconcile different views in our understanding of thermal stress. A long-standing model asserts that stress causes protein misfolding and aggregation, and the so-called “proteotoxic stress” leads to an increased production of molecular chaperones (39, 40). Yet more recent results argue that cells form condensates as an adaptive strategy to respond to changes in the environment, and some proteins, including Pab1, respond to stress first by condensing and then once the stress is released, by being dispersed by chaperones (12).

Our findings necessitate the reinspection and extension of the proteotoxicity model. The current results provide support for a merged paradigm in which Pab1, and presumably other stress-condensing molecules, undergoes only partial unfolding during stress-induced condensation. We speculate that this may have multiple beneficial consequences, consistent with our observations here: creating opportunities for specificity of condensation which would not be available in the case of complete denaturation, reducing potential for toxicity due to nonspecific interactions, and simplifying the chaperone-mediated recovery of native protein fold upon the return to nonstress conditions. Additionally, the heterogeneity and specific partial unfolding events observed here for Pab1 from *S. cerevisiae* are also seen in our recent study examining adaptive condensation for thermophilic and psychrophile homologs after accounting for differences in their optimal growth temperatures (41). These findings further support the view that Pab1 condensation, promoted by environmentally triggered limited unfolding, has been conserved over evolutionary timescales.

## Materials and Methods

**Condensates Preparation.** Condensates were prepared by subjecting a 60  $\mu$ M Pab1 stock to the condensing conditions. After treatment, the samples were centrifuged at 15,800 g for 10 min. The supernatant was removed, and the

pelleted condensates were washed 2× by buffer under the same centrifugation condition. Samples were diluted 29-fold into D<sub>2</sub>O buffer ( $pD_{corrected}$  6.0, on ice) to initiate deuterium labeling. After 30 to 24,000 s of labeling, HDX was quenched by dropping the pH to 2.5. HDX was conducted on monomeric (soluble) Pab1 (pH 6.8, 30 °C), pH-induced (pH 4.50, 30 °C, 30 min.), and three temperature-induced condensates (pH 6.8 or pH 6.5, 46 °C, 20 min; pH 6.5 42 °C, 3 h; pH 6.5, 39 °C, overnight) (Fig. 2A).

**HDX Labeling.** We prepared two HDX replicates using proteins from cells grown separately (two bioreplicates). HDX was initiated by diluting samples 29-fold into D<sub>2</sub>O buffer (50 mM sodium phosphate, 100 mM NaCl, and  $pD_{corrected}$  6.00) on ice. For each state and each replicate, samples at HDX time points of 30 s, 400 s, 1,500 s, 6,000 s, 12,000 s, and 24,000 s were taken. Additional time points at  $t_{HDX} = 10$  s, 200 s, and 800 s were taken for some states/replicates (SI Appendix, Table S1).

At each time point, a quench buffer containing 600 mM glycine, pH 2.5, and 8 M urea was added at a 1:1 ratio to stop HDX and dissolve the condensates. The quenched sample was further diluted with buffer containing 600 mM glycine, pH 2.5, at a 2:1 ratio to arrive at a final urea concentration of 2.67 M to avoid denaturing the protease.

For condensate replicate 1, condensates were resuspended and aliquoted. Then, D<sub>2</sub>O buffer was added to each aliquot separately (SI Appendix, Fig. S2A). At corresponding HDX time points, quench buffer containing 600 mM glycine, pH 2.5, and 8 M urea was added at a 1:1 ratio to quench HDX and dissolve the condensates. The quenched sample was further diluted with buffer containing 600 mM glycine, pH 2.5, at a 2:1 ratio to arrive at a final urea concentration of 2.67 M.

For replicate 2, condensates were resuspended with a minimum amount of H<sub>2</sub>O buffer and then diluted into D<sub>2</sub>O buffer as a bulk HDX reaction; then, individual aliquots were removed and quenched at each time point using the same protocol as for the monomeric Pab1 (SI Appendix, Fig. S2A).

All-D (fully deuterated) control samples were labeled in 50 mM sodium phosphate and 100 mM NaCl,  $pD_{corrected}$  8, using the same protocol for other data points. For some stable regions including the  $\alpha$ -helix of RRM3 and the slow subpopulations for most peptides in the condensates, the control samples were not fully deuterated. To avoid confusion, we term these controls as "saturated" instead of "all-D".

**LC-MS.** LC-MS measurements were done as described in ref. 42.

**HDX-MS Data Analysis.** For assignment, MS/MS data were searched against a sequence database containing sequences of Pab1, protease, and other proteins running on the LC-MS system using SearchGUI software (CompOmics Group). Search settings: unspecific cleavage, precursor charge 1–8, isotopes 0–1, precursor m/z tolerance 10.0 ppm, fragment m/z tolerance 0.5 Da, no post-translational modifications, and peptide length 6–30. The result of the search was imported into PeptideShaker (CompOmics Group) and further processed by EXMS2 (<http://hx2.med.upenn.edu/EXMS/>) to generate a peptide list.

For HDX analysis, MS1 data together with peptide list were imported into HDExaminer 3.1 (Sierra Analytics) to fit peptide isotope distributions. For condensates where some peptides had distinct bimodal mass envelopes, the bimodal fitting option in the software was used to determine the mass centroids of two individual populations. Downstream analysis and plotting were performed with Jupyter Notebook. HDX data exported from HDExaminer were filtered by a confidence score  $\geq 0.88$  (0.8 for condensates formed at 42/39 °C due to lower S/N ratio) for analysis and plotting. For bimodality/heterogeneity analysis, a filter of peptide length  $\geq 9$  was applied to ensure enough separation of the spectra of two populations for a good bimodal fitting quality. The %Fast, when analyzed on the residue level, is calculated by averaging the %Fast's of the three shortest peptides covering each residue.

**DLS.** DLS measurements were done as described in ref. 9. Measurements were performed in DynaPro NanoStar (Wyatt Technology). Measurements were performed as a slow temperature ramp at 0.25 °C min<sup>-1</sup> continuously from 25 °C or 30 °C. All experiments unless noted were performed at 15 μM concentration in 20 mM 4-(2-Hydroxyethyl)piperazine-1-ethanesulfonic acid (HEPES), pH 6.4, with 150 mM KCl, 2.5 mM MgCl<sub>2</sub>, and either in the absence or presence of 1 mM DTT.  $T_{cond}$  is characterized as the temperature where  $R_h$  is twice the pretransition value ( $R_h \sim 5$  nm for Pab1,  $\sim 3$  nm for RRM123).

**Protein Expression and Purification.** Protein expression and purification protocols were adapted with modification from ref. 9. BL21 *Escherichia coli* cells transformed with an expression plasmid for N-terminally 8xHis-tagged protein constructs were grown in LB at 37 °C until the optical density at 600 nm (OD600) reached between 0.6 and 0.7. The flask was cooled down at room temperature for 30 min before being transferred to a 30 °C incubator. Isopropyl β-D-1-thiogalactopyranoside (IPTG) was added to a final concentration of 0.2 mM to induce protein expression. Bi-Cys mutant protein was expressed in Shuffle T7 competent *E. coli* cells (NEB, cat# C3026L), and cells were grown at 30 °C instead of 37 °C.

Cells were harvested after 4 h of induction and lysed by sonication on ice in buffer containing 20 mM HEPES, pH 6.7, 150 mM KCl, 5 mM imidazole, 1 mM phenylmethylsulfonyl fluoride (PMSF), and 0.1% Triton. Lysate was clarified at 13,000 g for 30 min and loaded onto a 5-mL HiTrap chelating HP column (Cytiva 17-0409) on a Bio-Rad FPLC system. Bound protein was eluted with an imidazole gradient. Fractions containing the target protein were pooled with β-mercaptoethanol and tobacco etch virus (TEV) protease and dialyzed into 20 mM HEPES pH 6.7, 150 mM KCl, and 10% glycerol to remove N-terminal TEV tags. TEV-cut fractions were pooled and loaded into two 1-mL HiTrap heparin HP columns (Cytiva 17040601) for removal of nucleic acid contaminants with elution over a KCl gradient. Protein concentration was measured by absorbance at 280 nm.

**NMR.** NMR data were acquired either on Bruker AVANCE IIIHD 600 or a Bruker AVANCE III 500 NMR spectrometer equipped with a room temperature TXI probe with Topspin 3. Samples were exchanged to buffer at indicated pH (20 mM HEPES at pH 6.8, 150 mM KCl, 2.5 mM MgCl<sub>2</sub>, 2 mM tris(2-carboxyethyl) phosphine (TCEP) or 50 mM sodium acetate at pH 5.2, 100 mM KCl, and 2 mM TCEP) and concentrated to >150 μM. The mixing time for CLEANEX-PM measurements was 200 ms. Data were inspected in Topspin and analyzed and plotted using NMRviewJ.

**Total-Soluble-Pellet (TSP) Assay and Cocondensing Measurements.** The TSP assay for determining the protein fraction in the condensate was adapted from ref. 9. Concentrated protein stocks were diluted into a buffer containing 20 mM HEPES, pH 6.4, with 150 mM KCl and 2.5 mM MgCl<sub>2</sub> to a final concentration of 10 μM. For cocondensing experiments, both proteins were at a concentration of 10 μM. The sample was incubated at 42 °C for 20 min or 46 °C for 10 min followed by centrifugation at 15,800 g for 10 min at 10 °C. The supernatant was collected as the soluble fraction sample. Buffer was added to the pellet to wash out residual supernatant, and the sample was centrifuged again under the same condition. After removing the supernatant, the pellet was resuspended in buffer as the pellet fraction sample. Total (T), soluble (S), and pellet (P) fractions were analyzed by SDS-PAGE.

**SAXS.** SAXS data were collected at the BioCAT beamline at the Advanced Photon Source (Argonne National Lab) using an in-line size exclusion chromatography - small angle X-ray scattering (SEC-SAXS) protocol adapted from ref. 43. A concentrated protein sample (~3 mg/mL) was injected into an SEC system with a GE Lifesciences Superdex-200 size-exclusion column running in 20 mM HEPES, pH 7.4, 150 mM KCl, and 2 mM DTT at room temperature. Data were collected and analyzed using RAW (44) and GNOM (45) with the  $R_g$  values obtained from the pair-distance distribution function,  $P(r)$ , that were calculated using an indirect Fourier transform of the scattering data. The simulated conformational ensembles were created using the Upside molecular dynamics algorithm (46–48). The source code, parameters, and usage examples for Upside can be obtained from <https://github.com/sosnicklab/upside2-md/> (49).

**Data, Materials, and Software Availability.** All data are included in the article, and/or SI Appendix. The raw mass spectrometry proteomics data have been deposited to the ProteomeXchange Consortium via the PRIDE partner repository with the dataset identifier PXD049463 (50). The raw data for SAXS, NMR and DLS are publicly available at <https://github.com/trsosnick/Pab1-Condensates-2024/tree/main> (51).

**ACKNOWLEDGMENTS.** We thank I. Gagnon, A. Zmyslowski, and M. Baxa for assistance in MS and protein expression; X. Peng for assistance in molecular dynamics simulations; and H. Yoo and J. Bard for useful discussions. This work

was supported by NIH grants GM148233 (T.R.S.), GM126547 (D.A.D. and T.R.S.), GM055694 (T.R.S.), GM127406 (D.A.D.), GM144278 (D.A.D.), F30ES032665 (H.G.), T32GMO07183 (B. Glick, P. Rice, Pls), and a grant from the NSF MCB 2023077 (T.R.S.) and the US Army Research Office W911NF-14-1-0411 (D.A.D.). Use of the Advanced Photon Source, an Office of Science User Facility, operated for the Department of Energy (DOE) Office of Science by Argonne National Laboratory, was supported by the DOE under Contract DEAC02-06CH11357.

Author affiliations: <sup>a</sup>Pritzker School of Molecular Engineering, University of Chicago, Chicago, IL 60637; <sup>b</sup>Department of Biochemistry and Molecular Biology, University of Chicago, Chicago, IL 60637; <sup>c</sup>Graduate Program in Biophysical Sciences, Division of Physical Sciences, University of Chicago, Chicago, IL 60637; <sup>d</sup>Division of Biological Sciences, University of Chicago, Chicago, IL 60637; and <sup>e</sup>Institute for Biophysical Dynamics, University of Chicago, Chicago, IL 60637

Author contributions: R.C., H.G., J.A.R., D.A.D., and T.R.S. designed research; R.C., H.G., D.N.K., J.S., J.A.R., and T.R.S. performed research; R.C., H.G., D.N.K., J.S., J.A.R., and T.R.S. analyzed data; and R.C., H.G., D.N.K., J.R.S., J.A.R., D.A.D., and T.R.S. wrote the paper.

1. V. Cherkasov *et al.*, Coordination of translational control and protein homeostasis during severe heat stress. *Curr. Biol.* **23**, 2452–2462 (2013).
2. S. Jain *et al.*, ATPase-modulated stress granules contain a diverse proteome and substructure. *Cell* **164**, 487–498 (2016).
3. N. Kedersha, P. Anderson, Stress granules: Sites of mRNA triage that regulate mRNA stability and translatability. *Biochem. Soc. Trans.* **30**, 963–969 (2002).
4. E. W. J. Wallace *et al.*, Reversible, specific, active aggregates of endogenous proteins assemble upon heat stress. *Cell* **162**, 1286–1298 (2015).
5. M. Kato *et al.*, Cell-free formation of RNA granules: Low complexity sequence domains form dynamic fibers within hydrogels. *Cell* **149**, 753–767 (2012).
6. A. Molliex *et al.*, Phase separation by low complexity domains promotes stress granule assembly and drives pathological fibrillization. *Cell* **163**, 123–133 (2015).
7. S. Elbaum-Garfinkle *et al.*, The disordered P granule protein LAF-1 drives phase separation into droplets with tunable viscosity and dynamics. *Proc. Natl. Acad. Sci. U.S.A.* **112**, 7189–7194 (2015).
8. T. M. Franzmann, S. Alberti, Protein phase separation as a stress survival strategy. *Cold Spring Harb. Perspect. Biol.* **11**, a034058 (2019).
9. J. A. Riback *et al.*, Stress-triggered phase separation is an adaptive, evolutionarily tuned response. *Cell* **168**, 1028–1040.e19 (2017).
10. X. Jin *et al.*, Effects of pH alterations on stress- and aging-induced protein phase separation. *Cell. Mol. Life Sci.* **79**, 380 (2022).
11. S. Kroschwald *et al.*, Different material states of Pub1 condensates define distinct modes of stress adaptation and recovery. *Cell Rep.* **23**, 3327–3339 (2018).
12. H. Yoo, J. A. M. Bard, E. V. Pilipenko, D. A. Drummond, Chaperones directly and efficiently disperse stress-triggered biomolecular condensates. *Mol. Cell* **82**, 741–755.e11 (2022).
13. O. P. de Melo Neto, N. Standart, C. M. de Sa, Autoregulation of poly(A)-binding protein synthesis *in vitro*. *Nucleic Acids Res.* **23**, 2198–2205 (1995).
14. E. O. Melo, R. Dhalia, C. M. de Sa, N. Standart, O. P. de Melo Neto, Identification of a C-terminal Poly(A)-binding Protein (PABP)-PABP Interaction Domain. *J. Biol. Chem.* **278**, 46357–46368 (2003).
15. J. Cavanagh, W. J. Fairbrother, A. G. Palmer III, N. J. Skelton, *Protein NMR Spectroscopy: Principles and Practice* (Academic press, 1996).
16. C. Del Mar, E. A. Greenbaum, L. Mayne, S. W. Englander, V. L. Woods, Structure and properties of  $\alpha$ -synuclein and other amyloids determined at the amino acid level. *Proc. Natl. Acad. Sci. U.S.A.* **102**, 15477–15482 (2005).
17. S. W. Englander, L. Mayne, Y. Bai, T. R. Sosnick, Hydrogen exchange: The modern legacy of Linderström-Lang. *Protein Sci.* **6**, 1101–1109 (1997).
18. Y. Bai, J. S. Milne, L. Mayne, S. W. Englander, Primary structure effects on peptide group hydrogen exchange. *Proteins* **17**, 75–86 (1993).
19. N. Seetaloo, M. Zacharopoulou, A. D. Stephens, G. S. Kaminski Schierle, J. J. Phillips, Millisecond hydrogen/deuterium-exchange mass spectrometry approach to correlate local structure and aggregation in  $\alpha$ -synuclein. *Anal. Chem.* **94**, 16711–16719 (2022).
20. E. E. Boczek *et al.*, HspB8 prevents aberrant phase transitions of FUS by chaperoning its folded RNA-binding domain. *eLife* **10**, e69377 (2021).
21. D. Ubbiali *et al.*, Direct observation of “elongated” conformational states in  $\alpha$ -synuclein upon liquid–liquid phase separation. *Angew. Chem. Int. Ed.* **61**, e202205726 (2022).
22. Y. Liu *et al.*, Redox-mediated regulation of an evolutionarily conserved cross- $\beta$  structure formed by the TDP43 low complexity domain. *Proc. Natl. Acad. Sci. U.S.A.* **117**, 28727–28734 (2020).
23. C. Sahin *et al.*, Mass spectrometry of RNA-binding proteins during liquid–liquid phase separation reveals distinct assembly mechanisms and droplet architectures. *J. Am. Chem. Soc.* **145**, 10659–10668 (2023).
24. S. W. Englander, T. R. Sosnick, J. J. Englander, L. Mayne, Mechanisms and uses of hydrogen exchange. *Curr. Opin. Struct. Biol.* **6**, 18–23 (1996).
25. Z. Zhang, D. L. Smith, Determination of amide hydrogen exchange by mass spectrometry: A new tool for protein structure elucidation: Amide hydrogen exchange by mass spectrometry. *Protein Sci.* **2**, 522–531 (1993).
26. L. Mayne *et al.*, Many overlapping peptides for protein hydrogen exchange experiments by the fragment separation-mass spectrometry method. *J. Am. Soc. Mass Spectrom.* **22**, 1898–1905 (2011).
27. M. Källberg *et al.*, Template-based protein structure modeling using the RaptorX web server. *Nat. Protoc.* **7**, 1511–1522 (2012).
28. C. Maris, C. Dominguez, F.H.-T. Allain, The RNA recognition motif, a plastic RNA-binding platform to regulate post-transcriptional gene expression. *FEBS J.* **272**, 2118–2131 (2005).
29. H. Yoo, C. Triandafyllou, D. A. Drummond, Cellular sensing by phase separation: Using the process, not just the products. *J. Biol. Chem.* **294**, 7151–7159 (2019).
30. T.-L. Hwang, S. Mori, A. J. Shaka, P. C. M. van Zijl, Application of phase-modulated CLEAN chemical exchange spectroscopy (CLEANEX-PM) to detect water–protein proton exchange and intermolecular NOEs. *J. Am. Chem. Soc.* **119**, 6203–6204 (1997).
31. D. W. Oxtoby, D. Kashchiev, A general relation between the nucleation work and the size of the nucleus in multicomponent nucleation. *J. Chem. Phys.* **100**, 7665–7671 (1994).
32. J. J. De Yoreo, P. G. Vekilov, Principles of crystal nucleation and growth. *Rev. Mineral. Geochem.* **54**, 57–93 (2003).
33. H. Roder, G. A. Elöve, S. W. Englander, Structural characterization of folding intermediates in cytochrome c by H-exchange labelling and proton NMR. *Nature* **335**, 700–704 (1988).
34. L. Hoang, S. Bédard, M. M. Krishna, Y. Lin, S. W. Englander, Cytochrome c folding pathway: Kinetic native-state hydrogen exchange. *Proc. Natl. Acad. Sci. U.S.A.* **99**, 12173–12178 (2002).
35. G. Yao *et al.*, PAB1 self-association precludes its binding to poly(A), thereby accelerating CCR4 deadenylation *in vivo*. *Mol. Cell.* **27**, 6243–6253 (2007).
36. Y. Lin, D. S. W. Proter, M. K. Rosen, R. Parker, Formation and maturation of phase-separated liquid droplets by RNA-binding proteins. *Mol. Cell* **60**, 208–219 (2015).
37. T. S. Harmon, A. S. Holehouse, M. K. Rosen, R. V. Pappu, Intrinsically disordered linkers determine the interplay between phase separation and gelation in multivalent proteins. *eLife* **6**, e30294 (2017).
38. T. Mittag, R. V. Pappu, A conceptual framework for understanding phase separation and addressing open questions and challenges. *Mol. Cell* **82**, 2201–2214 (2022).
39. S. Lindquist, The heat-shock response. *Annu. Rev. Biochem.* **55**, 1151–1191 (1986).
40. R. I. Morimoto, Proteotoxic stress and inducible chaperone networks in neurodegenerative disease and aging. *Genes Dev.* **22**, 1427–1438 (2008).
41. S. K. Kik *et al.*, An adaptive biomolecular condensation response is conserved across environmentally divergent species. *bioRxiv* [Preprint] (2023). <https://doi.org/10.1101/2023.07.28.551061>. 12 November 2023.
42. A. M. Zmyslowski, M. C. Baxa, I. A. Gagnon, T. R. Sosnick, HDX-MS performed on BtuB in *E. coli* outer membranes delineates the luminal domain's allostery and unfolding upon B12 and TonB binding. *Proc. Natl. Acad. Sci. U.S.A.* **119**, e2119436119 (2022).
43. J. A. Riback *et al.*, Innovative scattering analysis shows that hydrophobic disordered proteins are expanded in water. *Science* **358**, 238–241 (2017).
44. J. B. Hopkins, R. E. Gillilan, S. Skou, *BioXTAS RAW*: Improvements to a free open-source program for small-angle X-ray scattering data reduction and analysis. *J. Appl. Crystallogr.* **50**, 1545–1553 (2017).
45. D. I. Svergun, Determination of the regularization parameter in indirect-transform methods using perceptual criteria. *J. Appl. Crystallogr.* **25**, 495–503 (1992).
46. J. M. Jumper, N. F. Faruk, K. F. Freed, T. R. Sosnick, Accurate calculation of side chain packing and free energy with applications to protein molecular dynamics. *PLoS Comput. Biol.* **14**, e1006342 (2018).
47. J. M. Jumper, N. F. Faruk, K. F. Freed, T. R. Sosnick, Trajectory-based training enables protein simulations with accurate folding and Boltzmann ensembles in cpu-hours. *PLoS Comput. Biol.* **14**, e1006578 (2018).
48. X. Peng *et al.*, Prediction and validation of a protein's free energy surface using hydrogen exchange and (importantly) its denaturant dependence. *J. Chem. Theory Comput.* **18**, 550–561 (2022).
49. J. M. Jumper, N. F. Faruk, K. F. Freed, T. R. Sosnick, Upside: Coarse-grained molecular dynamics for protein physics. <https://github.com/sosnicklab/upside2-md/>. Deposited 29 October 2014.
50. R. Chen, H. Glauinger, T. R. Sosnick, HDX-MS finds that partial unfolding with sequential domain activation controls condensation of a cellular stress marker. *ProteomeXchange* via the PRIDE database. <https://proteomecentral.proteomexchange.org/cgi/GetDataset?ID=PXD049463>. Deposited 18 February 2024.
51. R. Chen *et al.*, Data for “HDX-MS finds that partial unfolding with sequential domain activation controls condensation of a cellular stress marker.” GitHub. <https://github.com/trsosnick/Pab1-Condensates-2024/tree/main>. Deposited 28 February 2024.